

Corey K. Potvin<sup>\*1</sup>, Alan Shapiro<sup>1</sup>, Tian-You Yu<sup>2</sup>, Jidong Gao<sup>3</sup> and Ming Xue<sup>1,3</sup>

<sup>1</sup>School of Meteorology, University of Oklahoma, Norman, OK

<sup>2</sup>School of Electrical and Computer Engineering, University of Oklahoma, Norman, OK

<sup>3</sup>Center for Analysis and Prediction of Storms, Norman, OK

## 1. INTRODUCTION

A major focus in severe weather research for operational applications is the development of techniques to detect mesocyclones and tornadoes in real-time. Several factors limit the success of such techniques. First, a significant portion of the lower troposphere, within which tornadoes and low-level mesocyclones occur, is unobserved by the current Weather Surveillance Radar-1988 Doppler (WSR-88D) network (Maddox et al. 2002). Second, the degradation of azimuthal resolution with distance from the radar limits our ability to observe fine-scale features of significant circulations that do occur within the WSR-88D domain. Finally, the nearly complete lack of overlapping operational radar coverage at low levels prevents the application of multiple-Doppler techniques.

The National Science Foundation (NSF) Collaborative Adaptive Sensing of the Atmosphere (CASA) Engineering Research Center is exploring the feasibility of a nationwide network of low-cost, low-power, densely spaced X-band radars which would reduce the gaps in spatial coverage of the current WSR-88D system (McLaughlin et al. 2005). These radars would adaptively scan the lower troposphere based on a variety of end-user interests, including the forecaster's need to focus on severe and hazardous meteorological phenomena such as thunderstorms and regions of rotation. The method presented herein is designed to utilize the increased radar data resolution and coverage provided by a CASA-like network to detect and characterize tornadoes using a new multiple-Doppler vortex retrieval technique.

Multiple-Doppler wind retrieval techniques take advantage of the additional information gained by sampling a wind field from more than one radar perspective. Traditional methods consider the geometrical relation between two or more scanning radars and the radial wind field in order to retrieve the horizontal

wind field, and may also use the mass

---

\* Corresponding Author Address: Corey Potvin, 120 David L. Boren Blvd. Suite 5900, Norman, OK 73072; email: corey.potvin@ou.edu.

conservation equation to estimate the vertical velocity component. Variational multiple-Doppler techniques can employ additional constraints including background fields (e.g. Gao et al. 1999) and the anelastic vertical vorticity equation (Mewes and Shapiro 2002). A major advantage of variational techniques is that observations can be processed at the locations (and, in the case of 4D variational techniques, times) they occur, thereby eliminating error due to interpolation, moving reference frames or other ad hoc procedures commonly used in traditional dual-Doppler analysis. The technique presented herein shares this advantage.

In addition to the generic methods discussed above, single- and dual-Doppler techniques have been developed to retrieve the three-dimensional velocity field of a specific class of meteorologically significant flows: intense vortices. The Velocity Track Display (VTD; Lee et al. 1994) airborne radar data analysis method performs a harmonic analysis of single-Doppler data collected on successive flight legs over a tropical cyclone. In this method, Doppler winds on constant radius (as measured from the tropical cyclone center), constant-altitude rings are decomposed into the tangential, mean radial and mean cross-track components of the horizontal flow. The Ground-Based VTD (GBVTD; Lee et al. 1999) method has been used to examine the three-dimensional structure of a tornado sampled by a Doppler-on-Wheels radar (Lee and Wurman 2005). Unfortunately, successful application of the GBVTD method requires that the location of the vortex center be well known, a condition that is rarely met in stationary (even CASA-like) radar networks.

Since the implementation of the WSR-88D network, several algorithms have been developed to aid forecasters in real-time identification of intense small and mesoscale vortices, including the National Severe Storms Laboratory (NSSL) Mesocyclone Detection Algorithm (MDA; Stumpf et al. 1998) and the NSSL Tornado Detection Algorithm (TDA; Mitchell et al. 1998). Unfortunately, these approaches are very sensitive to the chosen shear thresholds, the suitability of which is

largely situation-dependent. More recent vortex detection approaches include neural network methods (Marzban and Stumpf 1996), the linear least squares derivative (LLSD) technique for estimating radial and divergent shear in Doppler velocity data (Smith and Elmore 2004), fuzzy-logic methods (e.g., Wang et al. 2005), multi-scale wavelet analysis of radial velocity data (Liu et al. 2006) and characterization of tornado spectral signatures (Yu et al. 2007).

In this study, radial wind observations from two or more close-proximity Doppler radars with overlapping domains are fit to an analytical low-order model of a vortex and near-environment. The model control parameters include vortex location, size, intensity, and translation velocity. The model parameters are retrieved by minimizing a cost function which measures the discrepancy between the observed and model radial wind fields.

The low-order wind model is introduced in section 2. The computation and minimization of the cost function is described in section 3. The simulation of the observation datasets used to test the technique is described in section 4. Highlights of the tests with analytically-generated data are discussed in section 5, and tests with a high-resolution Advanced Regional Prediction System (ARPS; Xue et al. 2001) dataset of a tornado vortex and mesocyclone are presented in section 6. Results of tests using real WSR-88D data of the 8 May 2003 tornadoes in central Oklahoma are presented in section 7. A summary follows in section 8.

## 2. DESCRIPTION OF LOW-ORDER MODEL

The vortex model used in this study is comprised of four idealized flow fields: a uniform flow, linear shear flow, linear divergence flow, and modified combined Rankine vortex (representing the tornado). The vortex and its environment are allowed to translate. Vertical shear is not accounted for in the model at this time, but will be implemented in the future. In the meantime, however, because of the small elevation angles and analysis subvolumes used in our experiments, there is minimal aliasing of vertical shear into horizontal shear. A total of 15 parameters are introduced to characterize the wind field in our low-order model. The model parameters are considered constant over a single 4D retrieval domain.

The Cartesian components of the linear flow fields (broad-scale flow) are given by

$$\begin{aligned} V_x &= a + b(y - v_t t) + c(x - u_t t), \\ V_y &= d + e(x - u_t t) + f(y - v_t t), \end{aligned} \quad (1)$$

where  $a, d$  are constant flow components,  $b, e$  are shear parameters,  $c, f$  are divergence parameters, and  $u_t, v_t$  the translational velocity of the broad-scale fields. It can be noted that (1) implicitly makes provision for a broad-scale vortex since the Cartesian representation of a solid body vortex is  $u = -\Omega y, v = \Omega x$ , where  $\Omega$  is the vortex angular velocity. This broad-scale vortex description is independent of the small-scale vortex model to be described next.

In a local cylindrical coordinate system centered on and translating with the modified combined Rankine vortex, the azimuthal velocity field  $v_\theta$  and radial velocity field  $v_r$  are given by:

$$\begin{aligned} v_\theta &= \begin{cases} \frac{r}{R} V_T & r < R \\ \frac{R^\alpha}{r^\alpha} V_T & r \geq R \end{cases}, \\ v_r &= \begin{cases} \frac{r}{R} V_R & r < R \\ \frac{R^\beta}{r^\beta} V_R & r \geq R \end{cases}, \end{aligned} \quad (2)$$

where

$$r = \sqrt{(x - x_0 - u_t t)^2 + (y - y_0 - v_t t)^2}, \quad (3)$$

is the distance of a given  $(x, y)$  coordinate from the center of the vortex at time  $t$ . The vortex is described by seven parameters: initial vortex center location  $(x_0, y_0)$ , radius of maximum wind  $R$ , maximum tangential velocity  $V_T$ , maximum radial velocity  $V_R$ , and the radial decay rates  $\alpha, \beta$  of the tangential and radial wind components. The translational velocity components  $u_t, v_t$  are the same as in the broad-scale model (1). The model parameters are listed in [Table 1](#).

The vortex equations are transformed into a Cartesian coordinate system as follows. The total velocity  $\mathbf{V}$  is decomposed into its radial and tangential components,  $\mathbf{V} = v_r \hat{r} + v_\theta \hat{\theta}$ , where

$\hat{r}$  and  $\hat{\theta}$  are the unit vectors in the radial and azimuthal directions (vortex cylindrical coordinates), respectively. [Figure 1](#) depicts the relationship between the Cartesian and vortex coordinate systems. The Cartesian components of  $\mathbf{V}$  are computed by taking the dot product of  $\mathbf{V}$  with each of the Cartesian unit vectors  $\hat{i}$  and  $\hat{j}$ :

$$\begin{aligned} u &= \hat{i} \cdot \mathbf{V} = v_r \cos \theta - v_\theta \sin \theta, \\ v &= \hat{j} \cdot \mathbf{V} = v_r \sin \theta + v_\theta \cos \theta. \end{aligned} \quad (4)$$

Formulae for  $\cos \theta$  and  $\sin \theta$  at arbitrary time  $t$  follow immediately from [Figure 1](#):

$$\begin{aligned} \cos \theta &= \frac{x - x_0 - u_t t}{r}, \\ \sin \theta &= \frac{y - y_0 - v_t t}{r}. \end{aligned}$$

Substituting these into (4) yields

$$\begin{aligned} u &= \frac{x - x_0 - u_t t}{r} v_r - \frac{y - y_0 - v_t t}{r} v_\theta, \\ v &= \frac{y - y_0 - v_t t}{r} v_r + \frac{x - x_0 - u_t t}{r} v_\theta. \end{aligned}$$

Substituting for  $v_r$ ,  $v_\theta$  from (2) and adding the linear flow fields (1) produces the Cartesian coordinates of the total wind field:

---


$$\begin{aligned} u &= \begin{cases} a + b(y - v_t t) + c(x - u_t t) + \frac{V_R}{R}(x - x_0 - u_t t) - \frac{V_T}{R}(y - y_0 - v_t t), & r < R, \\ a + b(y - v_t t) + c(x - u_t t) + \frac{R^\beta V_R (x - x_0 - u_t t)}{r^{\beta+1}} - \frac{R^\alpha V_T (y - y_0 - v_t t)}{r^{\alpha+1}}, & r \geq R, \end{cases} \\ v &= \begin{cases} d + e(x - u_t t) + f(y - v_t t) + \frac{V_R}{R}(y - y_0 - v_t t) + \frac{V_T}{R}(x - x_0 - u_t t), & r < R, \\ d + e(x - u_t t) + f(y - v_t t) + \frac{R^\beta V_R (y - y_0 - v_t t)}{r^{\beta+1}} + \frac{R^\alpha V_T (x - x_0 - u_t t)}{r^{\alpha+1}}, & r \geq R. \end{cases} \end{aligned}$$

Finally, solving for the radial component of the total velocity yields the model Doppler radar velocity,  $V_r^{mod}$ :

$$\begin{aligned} V_r^{mod} &= \left. \begin{aligned} &\cos \phi_n \sin \theta_n \left[ a + b(y - v_t t) + c(x - u_t t) + \frac{V_R}{R}(x - x_0 - u_t t) - \frac{V_T}{R}(y - y_0 - v_t t) \right] + \\ &\cos \phi_n \cos \theta_n \left[ d + e(x - u_t t) + f(y - v_t t) + \frac{V_R}{R}(y - y_0 - v_t t) - \frac{V_T}{R}(x - x_0 - u_t t) \right] \\ &r < R, \\ &= \cos \phi_n \sin \theta_n \left[ a + b(y - v_t t) + c(x - u_t t) + \frac{R^\beta V_R (x - x_0 - u_t t)}{r^{\beta+1}} + \frac{R^\alpha V_T (y - y_0 - v_t t)}{r^{\alpha+1}} \right] + \\ &\cos \phi_n \cos \theta_n \left[ d + e(x - u_t t) + f(y - v_t t) + \frac{R^\beta V_R (y - y_0 - v_t t)}{r^{\beta+1}} + \frac{R^\alpha V_T (x - x_0 - u_t t)}{r^{\alpha+1}} \right] \\ &r \geq R. \end{aligned} \right\} \quad (5) \end{aligned}$$

where  $\theta_n$  and  $\phi_n$  are the azimuth and elevation angles, respectively, of the  $n^{\text{th}}$  radar ( $\theta_n$  is measured clockwise from the north). In some of the experiments with analytically-generated data, a cylindrical approximation to the true spherical geometry was used. This approximation is justified by the small elevation angle ( $0.5^\circ$ ) used in these experiments.

### 3. COST FUNCTION COMPUTATION AND MINIMIZATION

The (squared) discrepancies between the observed and model-predicted wind fields are summed over the spatial-temporal domains of  $N$  radars, each scanning in range  $r_n$ , azimuth  $\theta$  and elevation angle  $\phi$ . Discrepancy calculations are performed at the same locations and times as the observations, so no spatial or temporal interpolation procedures are required.

Since radar resolution volumes increase in size with distance from the radar, Doppler velocity observations become representative of winds over a larger region as range increases. A range-weighting factor,  $r_n/r_{mean}$ , is introduced to account for this. In reality, radar resolution volumes increase as the square of range (spherical coordinate probe volumes), but in our experiments, resolution volumes are considered to be flat (cylindrical coordinate probe areas). However, it has been verified in other of our experiments (not shown) that the results are very similar regardless of which of these weighting functions is used.

The cost function  $J$  accounting for these discrepancies is

$$J \equiv \sum_{n=1}^N \sum_{m=1}^M \sum_{\phi} \sum_{\theta} \sum_{r_n} \frac{r_n}{r_{mean}} (V_r^{obs} - V_r^{mod})^2,$$

where  $M$  is the total number of volume scans (temporal sum) and  $r_n$  is the radial distance of a point from the  $n^{\text{th}}$  radar.  $J$  provides a useful way to quantitatively compare the quality of retrievals for different experiments, and, when appropriately normalized, can be used to calculate the mean range-weighted model error per radar gridpoint:

$$J_{norm} = \left\{ \frac{\sum_{n=1}^N \sum_{m=1}^M \sum_{\phi} \sum_{\theta} \sum_{r_n} \frac{r_n}{r_{mean}} (V_r^{obs} - V_r^{mod})^2}{\sum_{n=1}^N \sum_{m=1}^M \sum_{\phi} \sum_{\theta} \sum_{r_n} \frac{r_n}{r_{mean}}} \right\}^{1/2}$$

The cost function  $J$  is minimized to retrieve the set of parameter values producing the least squares error in the model wind (best fit between model and observed winds). In view of the location of the model parameters in (5), and the fact that discrepancies between the model and observations are squared in  $J$ , our minimization problem is highly non-linear. Conjugate gradient minimization methods have proven useful for such problems. The minimization algorithm used in this technique is the Polak-Ribiere (1969) method, a robust and efficient variant of the Fletcher and Reeves (1964) algorithm. In both methods, the search direction is reset to that of steepest descent (with all previous direction and gradient information discarded) every  $p$  iterations, where  $p$  is the number of model parameters.

In experiments with analytical or the ARPS-simulated data, the minimization algorithm was modified such that certain key model parameters are reset to their initial values if they exceed specified bounds. In particular,  $x_0$ ,  $y_0$  are reset whenever the provisional vortex center comes within a distance  $R$  (radius of maximum wind) of the edge of the analysis sub-domain (the reason is discussed in section 5). In addition,  $R$  is constrained to be larger than 10 m since vortices smaller than this are unlikely to be resolved by even a CASA-like radar network, and since negative values of  $R$  are physically impossible but could be obtained computationally. In experiments with WSR-88D data, retrievals are terminated if the provisional  $R$  becomes negative or if the provisional model vortex center comes within 500 m of the analysis subdomain boundary. Multiple analysis subdomains are used so that all possible vortex centers can be enclosed.

As with other minimization techniques, multiple minima in  $J$  can prevent the global minimum from being reached. Local minima in the current problem can result from the intrinsic non-linearity of the problem, as well as from areas of missing data and departures of the observed wind field from the model wind field.

The threat of local minima increases as the surface of the cost function becomes more

elliptical, since even small errors may be sufficient to produce spurious minima. In order to reduce the ellipticity of  $J$  and thus increase the convergence rate of the minimization algorithm, the first guess vector is scaled such that the gradients of  $J$  with respect to each of the parameters become closer in magnitude. To accomplish this, the scaling factors are set equal to physically realistic values of each of the parameters. Experiments have shown the technique to be relatively insensitive to the selection of scaling factors for physically reasonable ranges of these factors.

#### 4. ANALYTICALLY AND NUMERICALLY SIMULATED DATA

##### *a. Simulating the observations*

The low-order technique is tested using both analytically-generated vortices with surrounding broadscale flow and ARPS-simulated wind observations of a tornado and its near-environment. Observations in the analytical experiments were calculated from the low-order model, and thus represent an overly-optimistic (identical twin) framework. However, significant random errors were added to the analytical radial wind data in order to partially mitigate this problem. Both the idealized nature of the input wind field and the ability to specify the true wind parameter values facilitated testing of the algorithm code and identification of potential problems inherent to the technique. In contrast, the ARPS-simulated tornado is not constrained by the low-order model and therefore poses a greater challenge to the technique. On the other hand, there is some subjectivity in determining the size, intensity and location of the ARPS vortices. Data in the ARPS experiments are trilinearly-interpolated from the ARPS grid to the radar domain. Since the latter domain is generally coarser than the ARPS domain, the radial wind field sampled by the algorithm loses some of the finer features in the ARPS wind field, particularly at larger ranges from the radar.

To simulate weighted averaging of actual radar moment data within a resolution volume, simple range- and beam-weighting functions are applied to a distribution of hypothetical scatterers within each resolution volume in both the analytical and ARPS experiments. The range weight at a given point within the resolution volume is defined by a trapezoid function with value of unity between 20 m and 80 m along the beam and linearly decreasing to

zero at the edges of the resolution volume. This weighting function is similar to one used to emulate a WSR-88D range pattern (Wood et al. 2004). The azimuthal weight is given by

$$W_{az} = \exp \left[ -8 \ln 2 \left( \frac{\theta - \theta_0}{\theta_B} \right)^2 \right],$$

where  $\theta_0$  is the azimuth of the center of the beam and  $\theta_B$  is the half-power beamwidth, which is set to  $2^\circ$  in most of our ARPS experiments (to be consistent with the half-power beamwidth of the current CASA radars) and to  $1^\circ$  in the analytical experiments (to verify the code is free of error). The scanning strategy used in our experiments is further discussed in Section 4d.

##### *b. ARPS Simulation*

The numerically simulated supercell/tornado data used to test the algorithm were generated in a very high-resolution run of the ARPS model (case considered in Xue et al. 2006). The model thunderstorm was initiated by a thermal bubble placed in a homogeneous environment defined by a sounding proximate to the 20 May 1977 Del City, Oklahoma supercell storm (Ray et al. 1981). Computations were performed over a 48 km  $\times$  48 km domain with 50 m horizontal resolution and a stretched vertical resolution increasing from 20 m at the surface to about 80 m at 1 km AGL to 380 m at 16 km AGL. A simulation using a 25 m horizontal resolution (the one used in this study) was performed over a 30 min period centered on the time at which the 50 m grid tornado was most intense. The initial condition for the 25 m run consists of data interpolated from the 50 m grid. Due to the large storage requirement (over 100 MB) for each volume of data over the subdomain used in our retrieval experiments, only every 10 s of output data were made available to the algorithm. The data used in our retrieval experiments begin 13,200 s into the simulation (600 s after the initialization of the 25 m simulation). All references to time are relative to this 13,200 s simulation time. The ARPS model integration proceeded in a translating reference frame chosen to maintain the parent storm near the domain center throughout the duration of the simulation.

[Figure 2](#) shows the reflectivity field (based on rainwater mixing ratio) at the initial time ( $t = 290$  s after the beginning of our dataset) of some of our retrieval experiments. The tornado center

appears to be collocated with the minimum in the near-surface pressure field at  $x = 3925$  m,  $y = 4425$  m. This places the tornado along the leading edge of the hook echo signature, as is commonly observed. The tornado vortex is surrounded by a “donut” reflectivity pattern. [Figure 3](#) is a wind vector plot of the tornado and adjacent environment. A tornado-like vortex (hereafter referred to as a “tornado”) apparent near the center of the plot is embedded within a broader, weaker circulation. In the following we will use the pressure minimum to define the ARPS vortex location.

### *c. Scanning strategy*

The radar-vortex geometrical configuration used in our experiments with emulated observations (unless otherwise noted) is depicted in [Figure 4](#). Two radars are positioned to give a cross-beam angle of  $\sim 90^\circ$  at the location of the vortex. In experiments with the ARPS simulation, the tornado is located roughly 28 km from both radars, which are separated by 40 km (representative of a CASA radar network). In contrast, in the analytical experiments, a radar-vortex distance of  $\sim 7$  km was used. In the ARPS experiments, wind data are simultaneously valid over the spatial domain at each model time step and so each individual radar sector scan is assumed instantaneous on one elevation angle. In the analytical experiments, sector scans over a single elevation angle take 3.6 s. Unless stated otherwise, a return period of 30 s between three consecutive radar scans is used in both the analytical and ARPS experiments, giving a temporal domain of 70.8 s or 60 s, respectively. The radars sampled at 100 m range intervals, every  $0.5^\circ$  or  $1.0^\circ$  in azimuth, and over a single elevation angle of  $0.5^\circ$ . The beamwidth was set to  $1.0^\circ$  in the analytical experiments and in one set of ARPS experiments; a beamwidth of  $2.0^\circ$  was used in the remaining ARPS experiments.

### *d. First guess parameter values*

In the analytical experiments, first guess (FG) errors were typically set to +50 % of the true parameter values (see [Table 1](#)). The exception was the FG vortex center error, which was varied, and typically set in the range 0.5 km – 1.84 km.

In the experiments with ARPS data, the first guess for most parameters was set to zero. First guesses of 100 m, 0.7 and 0.7 were used for  $R$ ,  $\alpha$  and  $\beta$ , respectively. The FG vortex

center was typically placed 500 m or 1000 m east of the estimated ARPS tornado center.

## **5. MULTIPLE MINIMA IN ANALYTICAL EXPERIMENTS**

Experiments with analytical data demonstrated that multiple minima in  $J$  can occur even in wind fields exactly satisfying the low-order model. There are two reasons for this. First, local minima often occur near the edge of the analysis subdomain. Consequently, in experiments where the error in the first guess vortex center was large, the provisional vortex center tended to converge to a spurious minimum near or even outside of the analysis subdomain. This result motivated the practice in subsequent experiments of resetting the provisional vortex center to the first guess whenever it came within a certain range of the analysis subdomain boundary. It also demonstrated the need to use multiple first guesses for the vortex center in order to maximize the probability of detecting tornadoes when they are present. Second, the combination of the mathematical nature of the low-order model and the coarseness of the observational resolution produces non-uniqueness in the vortex parameters (particularly  $V_T$  and  $R$ ). Thus, retrieved vortices will often be either too large and weak or too small and intense.

## **6. EXPERIMENTS WITH ARPS DATA**

### *a. Two-step retrieval approach*

Preliminary experiments with ARPS data demonstrated that the tornadic circulation is more reliably retrieved when a two-step retrieval procedure is adopted. In step 1, the values of the vortex model parameters are fixed at zero (except for  $R$  since this would introduce a “division by zero” computational issue), and the broadscale parameters are retrieved. In step 2, the radial components of the wind field retrieved in step 1 are subtracted from the observed radial wind fields, and the retrieval is repeated on the residual wind field. Since the flow retrieved in step 1 (and subtracted in step 2) is much more representative of the broadscale flow than of the tornadic flow, the tornadic component of the original flow dominates the residual field to be retrieved in step 2. In order to make the retrieval more sensitive to the tornadic flow relative to the (presumably weaker) broadscale flow in step 2,

the cost at each observation point is multiplied by the square of the observed wind. This approach was also adopted in the experiments with the WSR-88D dataset (Section 7).

This two-step approach was often necessary to retrieve the tornado circulation when the tornado was in close proximity to the center of a non-tornadic, larger-scale circulation (low-level mesocyclone) present in the ARPS data. Large circulations may provide a better fit to the low-order model over the whole analysis domain than the smaller-scale tornado vortex. In these cases, a significant portion of the larger (and weaker) circulation is retrieved by the linear broadscale flow parameters in step 1, thereby increasing the probability that the tornadic circulation will be retrieved in step 2.

### *b. Results*

A series of retrievals was initiated at 30 s intervals over fifteen consecutive 60 s observation periods spanning a total window of 8 min. Each observation period consisted of 3 instantaneous radar scans, with scans obtained every 30 s. Only observations within a circular 1.5 km radius sub-domain centered on the FG vortex center were used. Retrieved wind fields were plotted and compared to the corresponding ARPS fields. The retrieved vortex parameter values were examined to determine how well they represented the simulated tornado. This determination was somewhat subjective for two reasons. First, since no mathematically rigorous definition of a tornado exists (see Lugt 1979 for a discussion of the difficulties inherent to defining vortices in general), there is no straightforward objective means of separating “tornadic” flow from “non-tornadic” flow. Furthermore, the ARPS-simulated tornado does not match the modified combined Rankine vortex model and so it would be impossible to assign “true” values to the vortex parameters in our retrievals even if the tornadic flow could somehow be distinguished from the rest of the wind field. As a result, comparisons between retrieved and expected (e.g. based on visual inspection of the ARPS wind field) values for the vortex parameters  $R$ ,  $V_T$ ,  $V_R$ ,  $\alpha$ , and  $\beta$  were not made. Retrieved values of the remaining vortex parameters ( $x_0$ ,  $y_0$ ,  $u_v$  and  $v_v$ ) could be more confidently assessed based on the location of the ARPS pressure minimum.

During the 8 min period over which this series of 15 retrievals was performed, the ARPS-simulated tornado becomes increasingly intense and distinct from the surrounding flow.

For much of the beginning of the test period, a non-tornadic circulation is located east of the tornado vortex within the analysis sub-domain, and a large portion of the flow surrounding both vortices is nearly as strong as the flow within the tornado vortex core. The FG for the vortex center was placed  $\sim 500$  m east of the tornado for the first set of tests discussed herein ( $t = 50$  s – 260 s); the FG error was increased to  $\sim 1000$  m in the second set of tests ( $t = 290$  s – 500 s), during which time the tornado was better defined and thus more amenable to retrieval (using the 1000 m FG error in the first set of experiments produced very poor retrievals due to the weakness of the simulated tornado at those early times).

Even with the 500 m error in FG vortex center location, the algorithm in some cases failed to retrieve the tornado. [Figure 5](#) shows the total ARPS wind field (top panel) and the retrieved vortex-only wind field (bottom panel) at  $t = 50$  s. The non-tornadic vortex to the east of the tornado is retrieved in this case rather than the tornado itself (the total wind field, not shown, is also well-retrieved). This result indicates the technique is able to detect relatively small, weak vortices, however, it also illustrates a potential cause for failure, as only one small-scale vortex can be retrieved in any single application of the algorithm. Even cursory inspection of [Figure 5](#) makes clear the difficulties inherent in retrieving a small weak tornado within a flow domain containing additional vortices of different sizes and strengths. It is therefore necessary that multiple first guesses for the vortex center be used in order to maximize the probability of detecting all tornadic vortices present.

By  $t = 290$  s, the simulated tornado has become sufficiently distinct from the surrounding flow to be detected by the algorithm using the 1000 m error FG vortex center. [Figure 6](#) illustrates the operation of the two-step retrieval procedure using this case as an example. Subtraction of the retrieved broadscale flow from the ARPS wind field removes a significant portion of the larger scale flow at this time, leaving behind a small-scale vortex in the residual field. The final retrieved vortex is roughly collocated with and somewhat larger than the ARPS tornado. The algorithm is evidently able to detect the simulated tornado and provide a reasonably good estimate of the total wind field even though the tornado is too weak to be visually discerned in the emulated radar moment data supplied to the algorithm ([Figure 7](#)).

In some cases, the retrieved vortex contained significant portions of both the tornado and the immediately adjacent flow (see [Figure 8](#)), making the retrieved vortex parameters less representative of the tornado itself. This resulted from the inability of the low-order model to sufficiently retrieve and subtract the non-tornadic flow in step 1. The retrieved maximum tangential wind occasionally significantly underestimated that of the simulated tornado ([Figure 9](#)), an effect which, along with overestimation of vortex radius, results in part due to limited observational resolution, which acts to smear finer-scale features (this effect was pointed out in the discussion of the analytical experiments). However, these biases also occur when the observed wind field violates the low-order model in such a way that portions of the larger-scale flow are recovered by the vortex parameters, as in the case just presented in [Figure 9](#).

The retrieved vortex and ARPS-estimated tornado paths over the temporal domain of the retrieval experiments are compared in [Figure 10](#). The latter path corresponds to the minimum in the ARPS pressure field near the height where observations were taken. The ARPS tornado center is defined by the location of this pressure minimum. The large eastward bias of the retrieved vortex location during the first half of the retrieval period has already been attributed to retrieval of a small-scale non-tornadic vortex east of the tornado. Between 290 s and 500 s, the estimated mean and maximum errors in retrieved vortex center were 156 m and 270 m, indicating that the method is skillful in identifying the location of the detected tornado.

Errors in the retrieved vortex translation parameters, as inferred from the ARPS-estimated tornado path, typically were not smaller than the errors obtained by computing the translation velocity from the retrieved vortex center at successive times and dividing by the retrieval time interval. Though of limited diagnostic value, these translation parameters model the actual tornado motion well enough that the initial vortex location and the remaining vortex parameters are better retrieved if vortex translation is included in the model.

It is possible that the results of these experiments would have improved had retrievals been performed for multiple first guess vortex centers and their results combined. Such an approach is used in the next set of experiments with real radar data. The experiments just discussed primarily serve to illustrate some of

the fundamental challenges the technique must overcome. The technique is adapted to address these challenges in the following section.

## 7. EXPERIMENTS WITH WSR-88D OBSERVATIONS

### *a. Description of Dataset*

The technique has most recently been tested using real multiple-Doppler data from a well-known, high-impact event. On 8 May 2003, a supercell produced an F0 tornado and then a longer-lived F4 tornado in the southern portion of the Oklahoma City, OK metropolitan area. The tornadoes remained within the observational domains of the KOKC (a Terminal Doppler Weather Radar) and KTLX radars (important characteristics of both radars are listed in [Table 2](#)) throughout their lifetimes, during which 0.5° elevation reflectivity and radial velocity scans were performed every ~5 min by KTLX and every ~1 min by KOKC. The tornado damage paths and relative locations of KOKC and KTLX are depicted in [Figure 11](#). A set of retrieval experiments was performed using data from seven consecutive 0.5° KTLX scans along with one 0.5° KOKC scan taken within ~30-60 s of each KTLX scan. The cross-beam angle in these experiments is least favorable (most acute) when the observed tornado is weakest, thereby presenting a notable challenge to the technique. All velocity data used in the experiments were subjectively de-aliased. The proximity of the tornado to both radars allowed observations to be collected at an azimuthal resolution characteristic of a CASA network. However, the range resolution of these data is much coarser than that for a CASA radar (~50-100 m), and the large time interval between KTLX 0.5° scans required that retrievals be performed on single pairs of KTLX/KOKC scans rather than using multiple consecutive scans from each radar. Thus, the retrievals obtained in these experiments are presumably representative of or slightly poorer than those which would have been obtained had the event been sampled by a CASA radar network.

### *b. Identification of regions of interest*

Using a sufficient number of analysis subdomains to cover the entire dual-Doppler domain would, in the absence of a high performance computing cluster, require too much time for the technique to be applied operationally. Therefore, the technique was

modified so that retrievals are performed only in regions identified as possibly containing intense vortices. The process by which these regions are selected begins by identifying all pairs of radar gates equidistant from the radar that satisfy the following criteria: (1) azimuthal shear of radial velocity calculated between the two radar gates exceeds  $.05 \text{ s}^{-1}$ ; (2) the maximum distance between the two gates is less than 1 km; (3) mean radial velocity exceeds  $25 \text{ ms}^{-1}$  in at least one of the gates; (4)  $<25 \%$  of the velocity data is missing within 500 m of each of the gates; and (5)  $<10 \%$  of the velocity data is missing within 1000 m of each of the radar gates. Criteria 1, 2 and 3 are intended to distinguish between tornado-like and weaker or broader vortices. Criteria 4 and 5 ensure that sufficient velocity data are available for retrievals to be representative of the actual wind field. These latter criteria were partly motivated by experiments in which velocity data gaps produced spurious minima in  $J$ .

For each pair of radar gates satisfying all seven criteria, the centroid of the two gates is stored. All such points subsequently found not to be located within 2 km of another such point in the other radar's domain are discarded. This is done to distinguish between vortices, which will exhibit azimuthal shear signatures in the velocity fields of both radars, and regions of strong linear shear. All retained points are then spatially grouped into clusters (since there may be multiple proximate points associated with the same vortex) whose centroids are calculated and stored.

Each centroid corresponds to the center of a region over which the retrieval technique is to be applied. A grid of first guesses for the vortex center (each serving as the center of an analysis subdomain over which the retrieval is applied) is subsequently calculated and input to the retrieval routine. In these experiments, nine first guesses separated by 500 m in both the x- and y-directions are used. The need to use multiple first guesses for the vortex center has already been discussed in sections 5 and 6.

Due to the coarseness of the observational resolution and the fact that tornadic wind fields depart from the low-order model, there appears to be no obvious way to identify the most accurate retrieved value of each parameter among each set of retrievals. Therefore, information from each set of retrievals (one set for each region of interest) is combined by taking the ensemble mean, maximum and minimum of each of the vortex parameters. The ensemble

mean is useful since it is a more reliable estimator than a randomly selected retrieved parameter value. Together, the maxima and minima provide a sense of the uncertainty in the ensemble mean values.

Since multiple intense vortices may exist within a single region of interest, groups of retrievals whose retrieved vortex centers are well-separated from the rest ( $\sim 1 \text{ km}$ ) are presumed to correspond to a different vortex and therefore have their statistics calculated separately. In the experiments presented herein, however, only one tornado is present and the technique correctly outputs a single set of mean vortex parameter values.

### *c. Detection Criteria*

Only retrievals which meet a set of detection criteria are used in the calculation of the vortex parameter ensemble statistics. The detection criteria used in these experiments have only been tested with the present dataset and therefore are considered preliminary. These criteria are as follows: (1)  $0.4 < \alpha < 1.5$ ; (2)  $|V_T/R| > 0.5 \text{ s}^{-1}$ ; and (3)  $|V_T| > 20 \text{ ms}^{-1}$ . Criterion (1) eliminates vortices whose region of intense winds is unrealistically narrow or overly broad (and therefore not tornado-like); (2) eliminates vortices which are likely more representative of a low-level mesocyclone than of the tornado (if one is present) itself; and (3) eliminates weaker, non-tornadic vortices.

### *d. Characterizations unsupported by observational data*

In some cases where the technique successfully detected the tornado, the retrieved  $R$  was too small relative to the observational resolution to be supported by the data. That is, the "true"  $R$  may well have been this small, but it was impossible to conclude this based on the available data. This issue results from the vortex parameter non-uniqueness problem discussed earlier, and is usually associated with a retrieved  $V_T$  that is high relative to retrievals with a larger value of  $R$ . In practice, bounds should be placed on the values of  $R$  or the maximum retrieved wind shear which can be resolved given the observational resolution. In this way, retrieved vortices which pass the detection criteria but are not well-sampled can be identified and interpreted with caution.

### *e. Spurious retrievals*

In one of the 63 retrievals performed in these experiments, the retrieved vortex was

located  $\sim 2$  km from and rotating oppositely to the actual tornado. This occurred because the broadscale flow was not well-retrieved in the first step of the retrieval, resulting in a residual wind field containing strong flow not directly associated with the tornado. This strong non-tornadic flow was subsequently captured by the spurious vortex. Fortunately, objective identification and rejection of this vortex could have easily been accomplished by comparing some characteristic (e.g. shear) between the retrieved and observed wind fields. The development of such an approach requires testing with additional datasets and is the subject of future work.

#### *f. Results*

As in the experiments with the ARPS tornado simulation, the first guess for most parameters in these experiments (other than  $x_0$  and  $y_0$ , which are determined by the identified regions of interest) was set to zero except for  $R$  ( $=100$  m),  $\alpha$  ( $=0.7$ ) and  $\beta$  ( $=0.7$ ). In all seven experiments (each one corresponding to a pair of KTLX/KOKC  $0.5^\circ$  elevation scans), the only region of interest identified by the criteria listed in Section 6b contained the tornado. This is a good result since no other tornado-like vortices existed in the radar domains, and so the technique did not waste computational resources. However, the suitability of these criteria will need to be further tested using additional tornado observation sets.

In all the experiments, the mean retrieved vortex center is located within or near the tornado damage path (Figure 12). There is considerable spread in the individual retrieved vortex centers, particularly in the first and last experiments (up to  $\sim 1$  km). This underscores the importance of the effects of multiple minima in the cost function. Similarly, there is significant variation in  $R$  and  $V_T$  among the retrievals for each experiment, which is not surprising in light of the vortex parameter non-uniqueness problem described previously. Given this consideration and the fact that the “true” values of these parameters are unknown, no attempt was made to evaluate the retrieved vortex parameters other than the vortex location. In future experiments, new characteristics which are more operationally useful and perhaps more easily verified will be calculated from the retrieval (e.g. retrieved region of potentially damaging winds). It should also be possible to assign a lower bound to the peak total winds in/near the tornado based on the data resolution

and characteristics of the observed and retrieved wind fields.

Comparison of the observed radial velocity field with that retrieved by the technique for a representative case indicates the low-order model is able to capture some of the complexity in the Doppler velocity field (Figure 13). Of course, the agreement between the true and retrieved Cartesian wind fields (Figure 14), particularly on scales finer than the observational resolution, is unknown in this case and, given the observed complexity (e.g. multiple vortices, inflow jets) in tornadoes, may be quite limited. However, despite the relative simplicity of the low-order model and the coarseness of the available data, the technique is still able to produce reasonable retrievals of the tornadic wind fields in these experiments.

## **8. SUMMARY**

A new multiple-Doppler technique for identifying and characterizing tornadoes has been presented. The method consists of fitting radial wind observations to a low-order model of a tornado-like vortex and its near environment. The technique takes advantage of the enhanced density (and therefore spatial coverage and resolution) of a CASA-like radar network. The retrieval technique has been tested against analytically-generated observations, a high-resolution ARPS simulation of a tornado and surrounding wind field, and WSR-88D observations of the 8 May 2003 Oklahoma City tornadoes. The technique exhibits skill not only in detecting tornado-like vortices within a CASA-like network, but also in retrieving their total wind field. Vortex characteristics derived from these retrievals may aid in the tornado warning process.

Spurious minima can pose a serious threat to the minimization algorithm’s ability to converge to the correct minimum. Minima in  $J(x_0, y_0)$  can occur due to data boundaries, vortex parameter non-uniqueness, and deviations of the observed wind pattern from that described by the low-order model. An important special case of such a deviation is the presence of multiple vortices. This local minima problem necessitates the use of multiple first guesses for the location of the vortex and of a two-step approach in which much of the larger-scale flow is retrieved and subtracted before the small-scale vortex retrieval is performed. The latter strategy is necessary in cases where a weaker and broader vortex-like circulation

provides a better fit to the low-order model over an analysis domain than a collocated intense vortex.

Due to real-time computational constraints, the algorithm is applied only to regions meeting an azimuthal radial wind shear threshold and other criteria. A grid of first guess vortex centers (and corresponding analysis subdomains) is defined in each region identified in this way. Retrievals are performed on each set of analysis subdomains and ensemble mean vortex parameter values computed for any vortices meeting the detection criteria. Additional tests with Doppler observations of tornadoes are necessary to refine the detection criteria and to develop approaches to rejecting spurious retrievals. Further testing is also required to assess the technique's performance in more challenging scenarios (e.g. smaller and/or weaker tornadoes or when Doppler velocity data are objectively, not subjectively, de-aliased). Finally, greater use will be made of quantities derived from the retrievals since these would likely provide more operationally useful information than the vortex parameters themselves, and may facilitate evaluation of the technique.

## 9. ACKNOWLEDGMENTS

Special thanks to Gordon Carrie for providing the software used to read the DORADE format data used herein. This work was supported by the Engineering Research Centers Program of the National Science Foundation under grant EEC-0313747.

## 10. REFERENCES

Fletcher, R., and C.M. Reeves, 1964: Function minimization by conjugate-gradients. *Computer J.*, **7**, 149-153.

Gao, J.-D., M. Xue, A. Shapiro, and K. K. Droegemeier, 1999: A variational method for the analysis of three-dimensional wind fields from two Doppler radars. *Mon. Wea. Rev.*, **127**, 2128-2142.

Lee, W.-C., and J. Wurman, 2005: Diagnosed three-dimensional axisymmetric structure of the Mulhall tornado on 3 May 1999. *J. Atmos. Sci.*, **62**, 2373-2393.

—, F. D. Marks, Jr., and R. E. Carbone, 1994: Velocity Track Display – A technique to extract real-time tropical cyclone circulations using a single airborne Doppler radar. *J. Atmos. Oceanic Technol.*, **11**, 337–356.

—, J.-D. Jou, P.-L. Chang, and S.-M. Deng, 1999: Tropical cyclone kinematic structure retrieved from single Doppler radar observations. Part I: Interpretation of Doppler velocity patterns and the GBVTD technique. *Mon. Wea. Rev.*, **127**, 2419-2439.

Liu, S., M. Xue, and Q. Xu, 2007: Using wavelet analysis to detect tornadoes from Doppler radar radial-velocity observations. *J. Atmos. Ocean Tech.*, **24**, 344-359.

Lugt, H. J., 1979: The dilemma of defining a vortex. *Recent Developments in Theoretical and Experimental Fluid Mechanics*, U. Mueller, K. G. Riesner and B. Schmidt, Eds., Springer-Verlag, 309–321.

Maddox, R. A., Zhang, J., Gourley, J. J., and Howard, K. W., 2002: Weather radar coverage over the contiguous United States. *Wea. Forecasting*, **17**, 927-934.

Marzban, C. and G. J. Stumpf, 1996: A neural network for tornado prediction based on Doppler radar-derived attributes. *J. Appl. Meteor.*, **35**, 617–626.

McLaughlin, D., V. Chandrasekar, K. Droegemeier, S. Frasier, J. Kurose, F. Junyent, B. Philips, S. Cruz-Pol, and J. Colom, 2005: Distributed Collaborative Adaptive Sensing (DCAS) for improved detection, understanding, and predicting of atmospheric hazards. Preprints, *85<sup>th</sup> AMS Annual Meeting*, San Diego, CA, Amer. Meteor. Soc.

Mitchell, E. D., Vasiloff, S. V., Stumpf, J. G., Witt, A., Eilts, M. D., Johnson, J. T., and K. W. Thomas, 1998: The National Severe Storms Laboratory Tornado Detection Algorithm. *Wea. Forecasting*, **13**, 352–366.

Polak, E. and G. Ribiere, 1969: Note sur la convergence de methodes de directions conjuguees. *Rev. Franc. Informat. Rech. Operationnelle*, **16**, 35-43.

Ray, P. S., B. C. Johnson, K. W. Johnson, J. S. Bradberry, J. J. Stephens, K. K. Wagner, R. B. Wilhelmson, and J. B. Klemp, 1981: The morphology of several tornadic storms on 20 May 1977. *J. Atmos. Sci.*, **38**, 1643-1663.

Smith, T. M., and K. L. Elmore, 2004: The use of radial velocity derivatives to diagnose rotation and divergence. Preprints, *11<sup>th</sup> Conf. on Aviation, Range and Aerospace*, Hyannis, MA, Amer. Meteor. Soc.

Stumpf, J. G., Witt, A., Mitchell, E. D., Spencer, P. L., Johnson, J. T., Eilts, M. D., Thomas, K. W., and D. W. Burgess, 1998: The National Severe Storms Laboratory

- Mesocyclone Detection Algorithm for the WSR-88D. *Wea. Forecasting*, **13**, 304-326.
- Wang, Y., T.-Y. Yu, M. Yeary, A. Shapiro, D. S. Zrnica, M. Foster and D. Andra, 2005: Tornado detection using the neuro-fuzzy method. Preprints, *32nd Conf. on Radar Meteorology*, Albuquerque, New Mexico, Amer. Meteor. Soc.
- Wood, V.T., D.C. Dowell, and R.A. Brown, 2004: Simulated WSR-88D measurements of a tornado having a weak reflectivity center. Preprints, *22<sup>nd</sup> Conf. on Severe Local Storms*, Hyannis, MA, Amer. Meteor. Soc.
- Xue, M., K. K. Droegemeier, V. Wong, A. Shapiro, K. Brewster, F. Carr, D. Weber, Y. Liu, and D. Wang, 2001: The Advanced Regional Prediction System (ARPS) – A multi-scale nonhydrostatic atmospheric simulation and prediction tool. Part II: Model physics and applications. *Meteor. Atmos. Phys.*, **76**, 143-165.
- , M., S. Liu, and T. Yu, 2006: Variational analysis of over-sampled dual-Doppler radial velocity data and application to the analysis of tornado circulations. *J. Atmos. Oceanic Technol.*, **24**, 403-414.
- Yu, T.-Y., Y. Wang, A. Shapiro, M. Yeary, D. Zrnica, and R. Doviak, 2007: Characterization of tornado spectral signatures using higher-order spectra. *J. Atmos. Oceanic Technol.*, **24**, 1997-2013.

**Table 1.** True values of low-order model parameters used in analytical retrievals, and results of a set of eight retrievals (EXP1) and one single retrieval (EXP2).

Parameter	True Value	Mean Retrieved Value (EXP1)	Standard Deviation (EXP1)	Retrieved Value (EXP2)
$a$ ( $m s^{-1}$ )	10	9.4	0.7	11.6
$b$ ( $s^{-1}$ )	.002	.0023	.0004	.0012
$c$ ( $s^{-1}$ )	.0015	.0019	.0002	.0010
$d$ ( $m s^{-1}$ )	10	9.4	0.4	11.2
$e$ ( $s^{-1}$ )	.002	.0021	.0004	.0024
$f$ ( $s^{-1}$ )	.002	.0024	.0004	.0014
$R$ (m)	200	202	11	309
$V_R$ ( $m s^{-1}$ )	-10	-9.9	1.0	-9.4
$V_T$ ( $m s^{-1}$ )	50	48.3	1.4	38.6
$x_0$ (m)	5000	4997	9	5003
$y_0$ (m)	5000	4998	10	4997
$u_t$ ( $m s^{-1}$ )	-10	-9.9	1.8	-10.1
$v_t$ ( $m s^{-1}$ )	-10	-10.0	1.6	-9.9
$\alpha$	0.7	.687	.056	0.75
$\beta$	0.4	.374	.135	0.78

**Table 2.** Selected characteristics of KOKC and KTLX.

	<b>Beamwidth</b>	<b>Azimuthal Sampling</b>	<b>Range Sampling</b>	<b>Doppler Band</b>
<b>KTLX</b>	0.95°	1.0°	250 m	S
<b>KOKC</b>	1.0°	1.0°	150 m	C

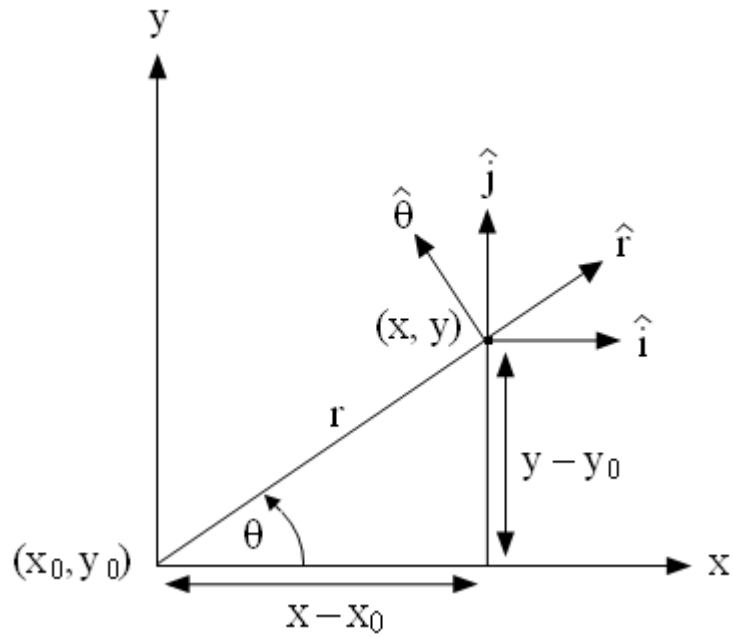


[Figure 1](#). Cartesian and cylindrical (vortex) coordinate systems defining model broadscale and vortex flows, respectively at  $t = 0$ . The vortex is initially located at  $x_0, y_0$ .

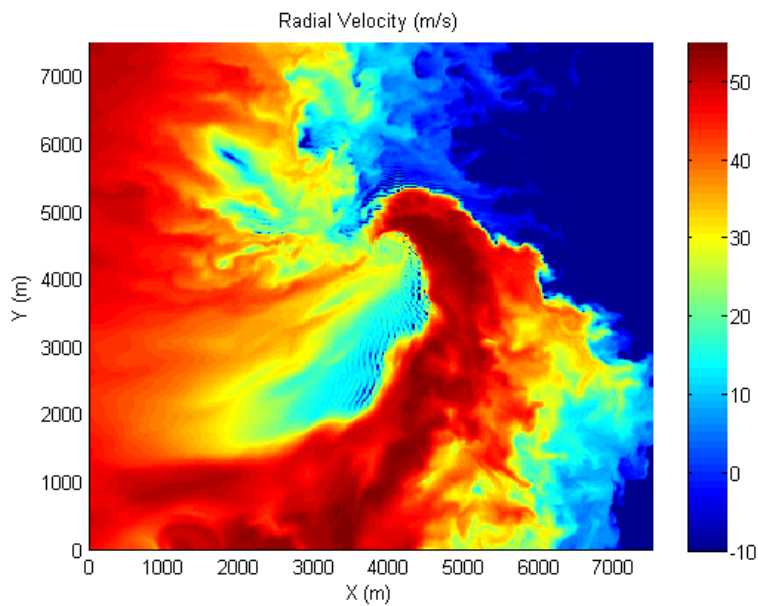


[Figure 2](#). ARPS reflectivity field (dBZ) at  $t = 290$  s.

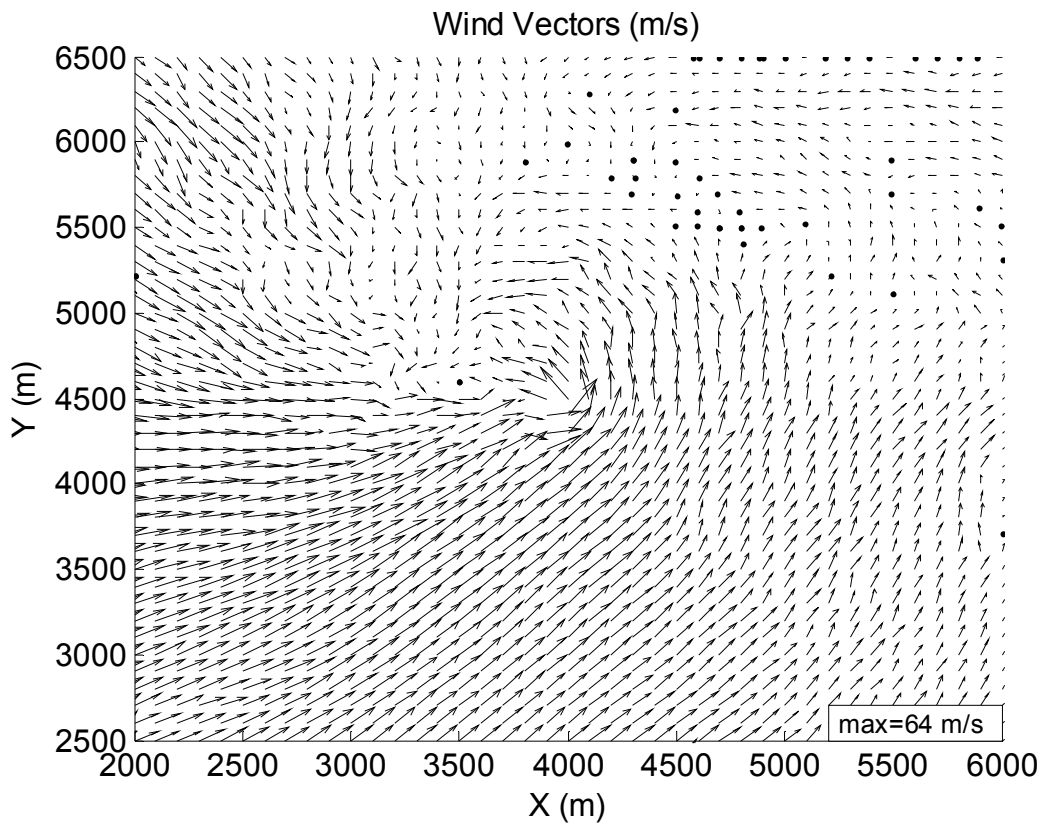


[Figure 3](#). Horizontal wind field in and around ARPS-simulated tornado at  $z = 108$  m and  $t = 290$  s. Only vectors at every fourth grid point are displayed.

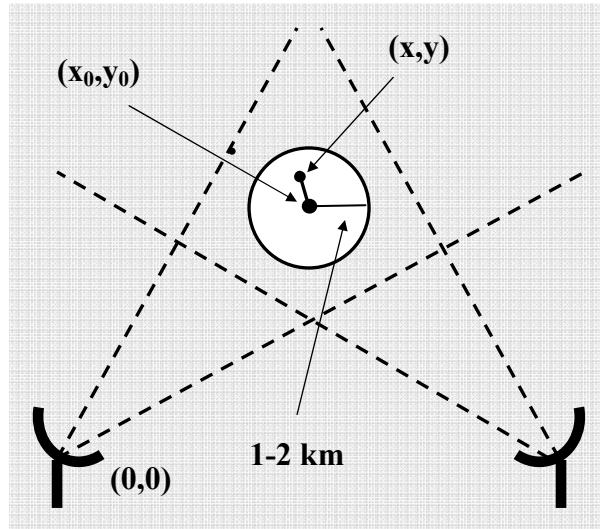


[Figure 4](#). Radar-vortex geometry and analysis domain.

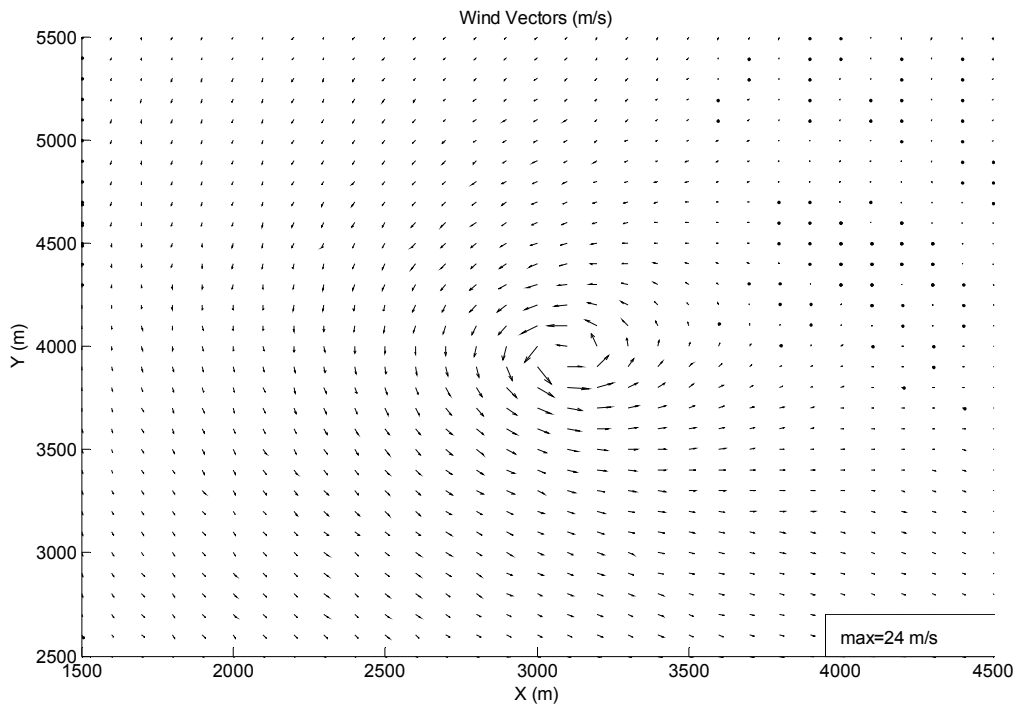
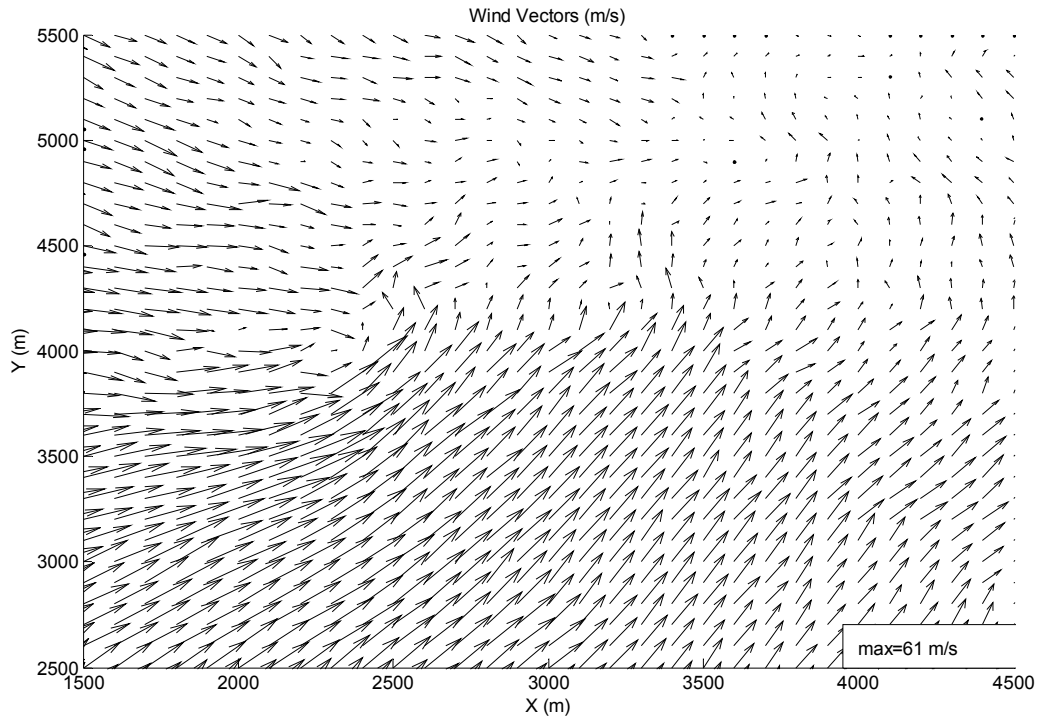


**Figure 5.** ARPS total (top) and retrieved vortex-only (bottom) wind fields at  $t = 50$  s. Every other vector omitted for readability. Plot domain circumscribes the 1.5 km radius circular analysis sub-domain used in the retrieval.

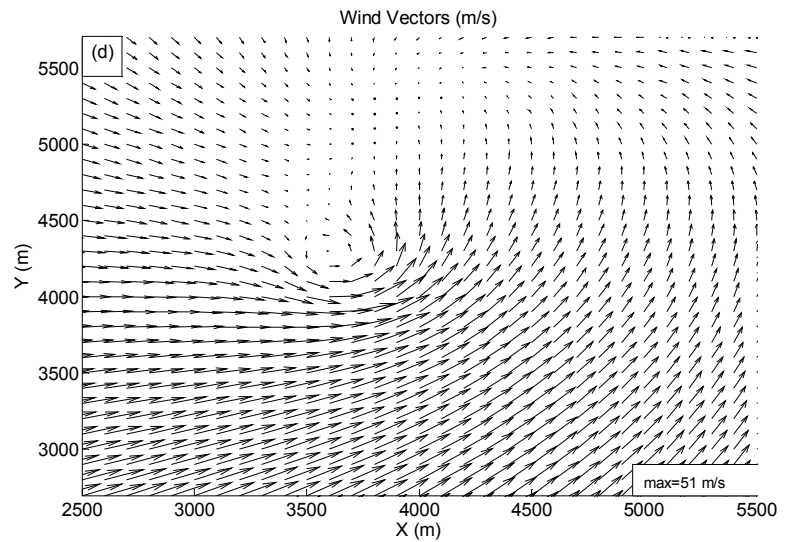
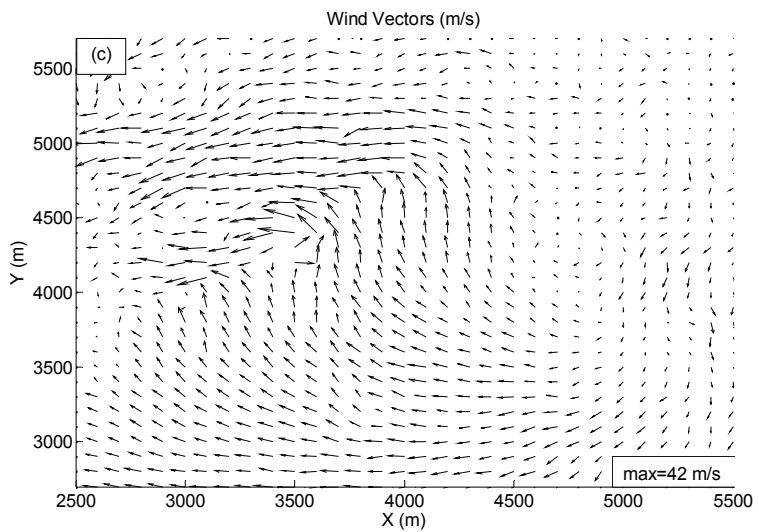
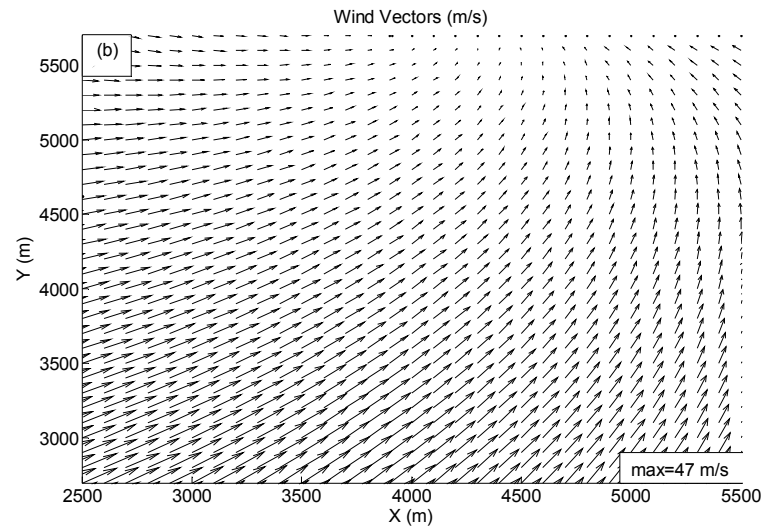
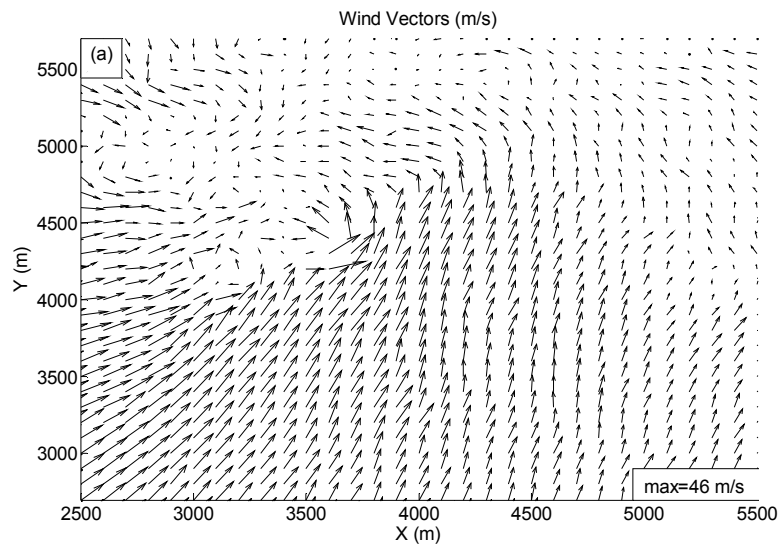


**Figure 6.** Illustration of two-step retrieval procedure, valid at  $t = 200$  s: (a) ARPS wind field, (b) retrieved broadscale flow, (c) the vector difference (a)-(b), and (d) total retrieved flow.

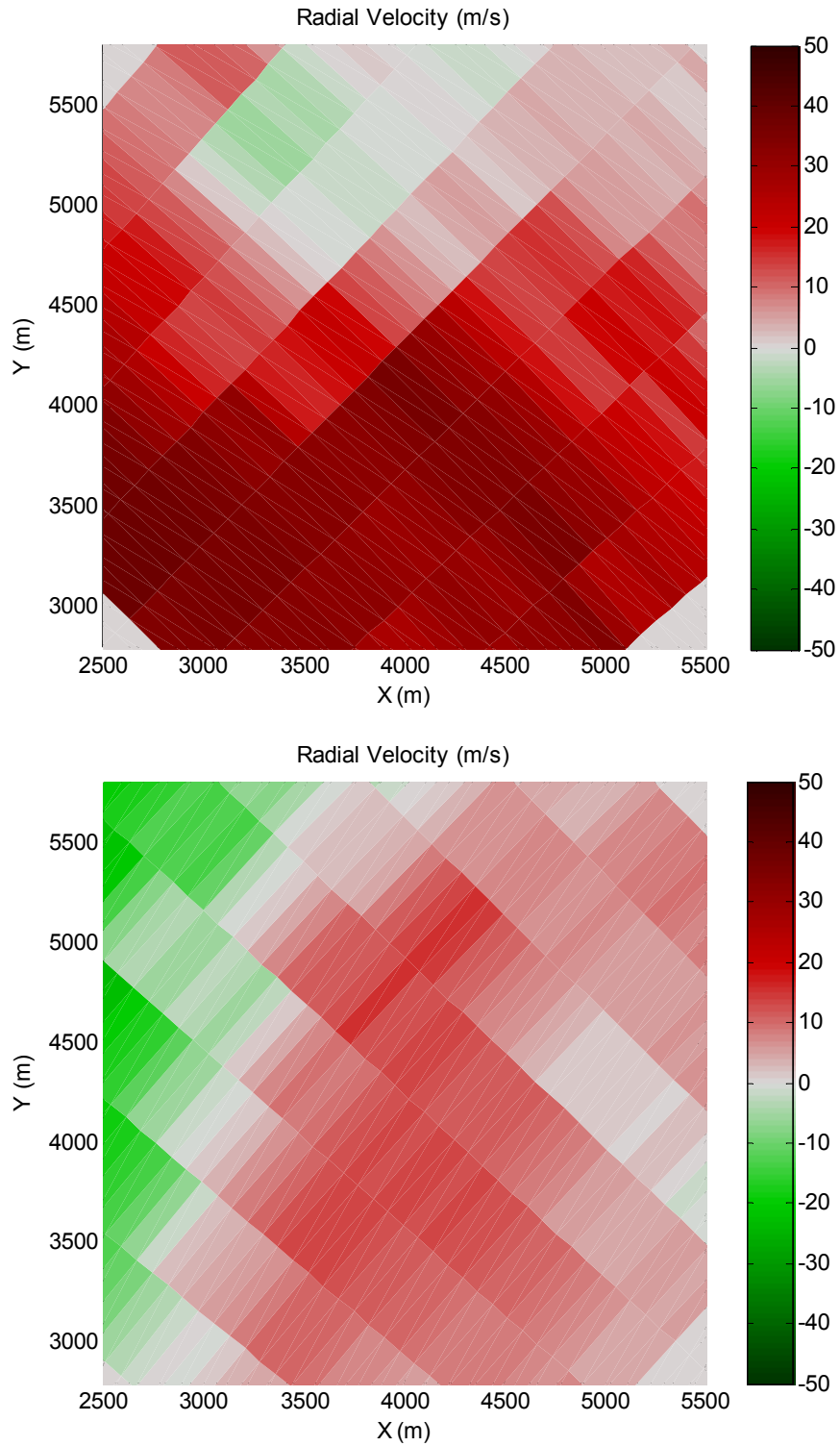


[Figure 7](#). Emulated radial velocity observations input to retrieval algorithm at  $t = 200$  s. (top)  $V_r$  from radar at  $x = -15$  km,  $y = -15$  km; (bottom)  $V_r$  from radar at  $x = 25$  km,  $y = -15$  km.

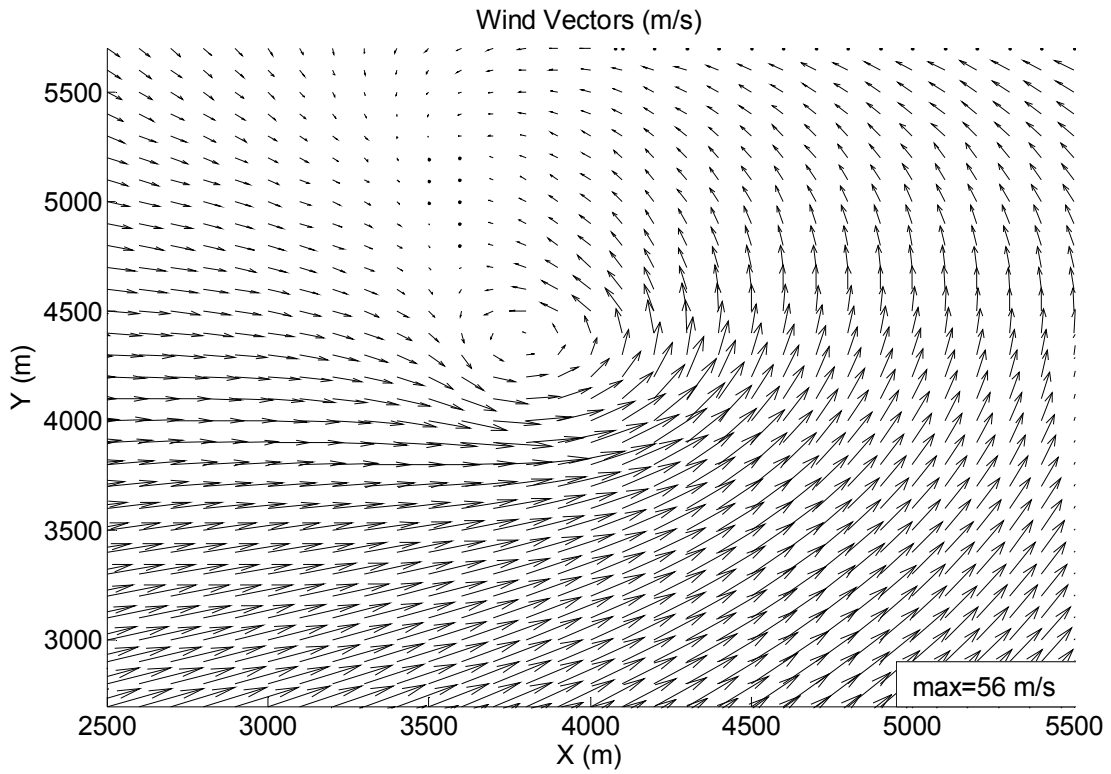
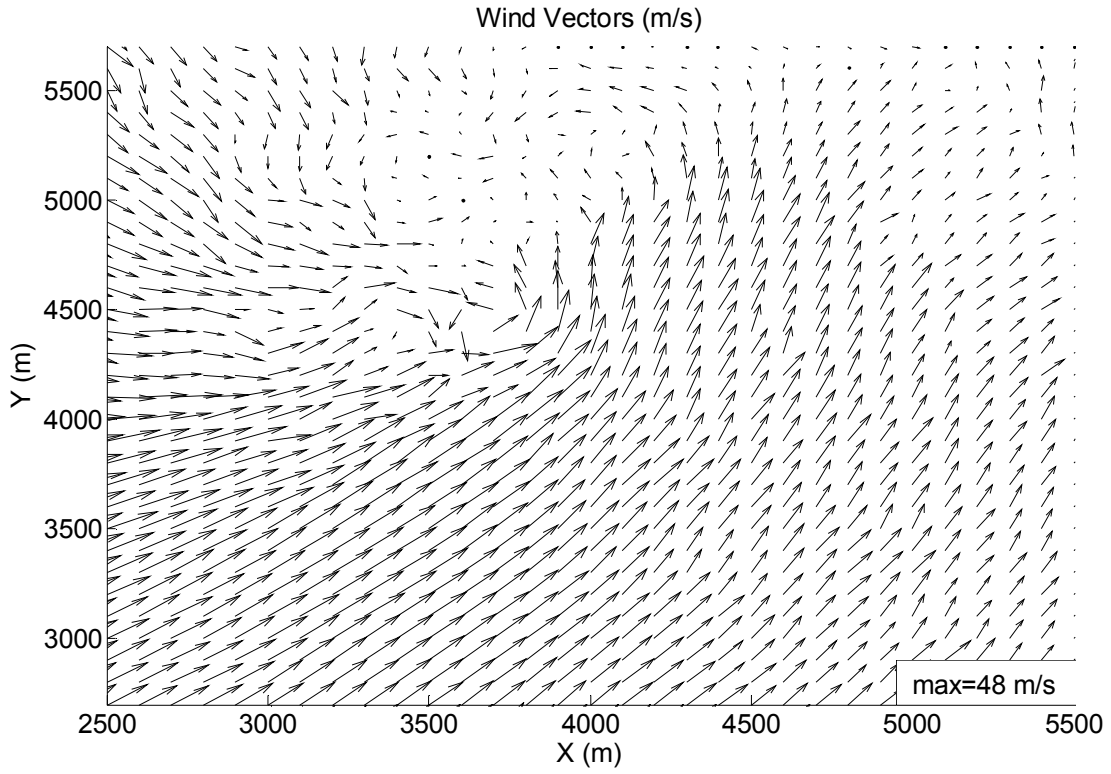


[Figure 8](#). ARPS (top) and retrieved (bottom) wind fields at  $t = 260$  s.

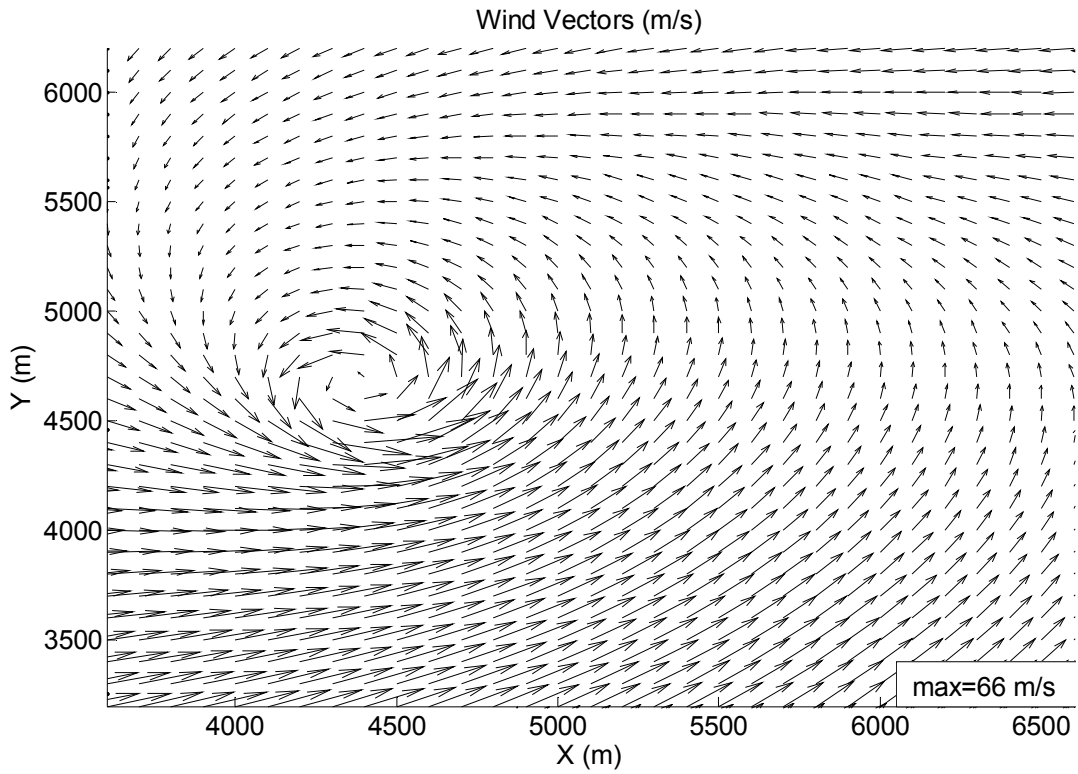
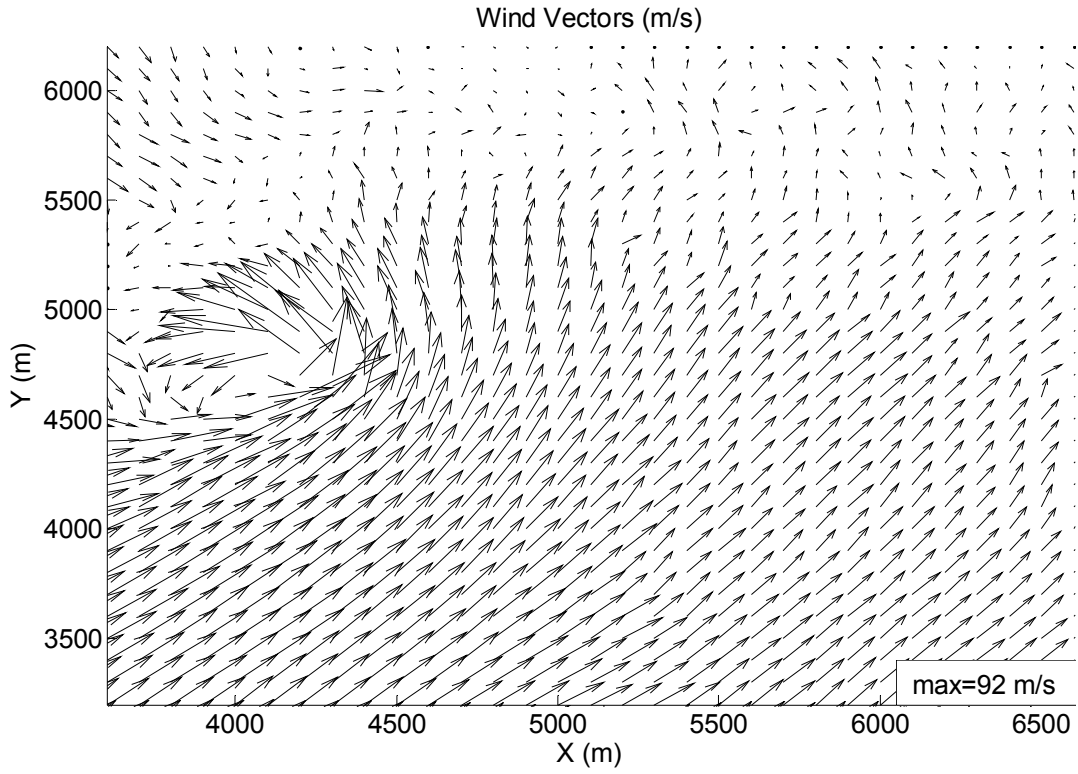


[Figure 9](#). As in Figure 10 but for  $t = 440$  s.

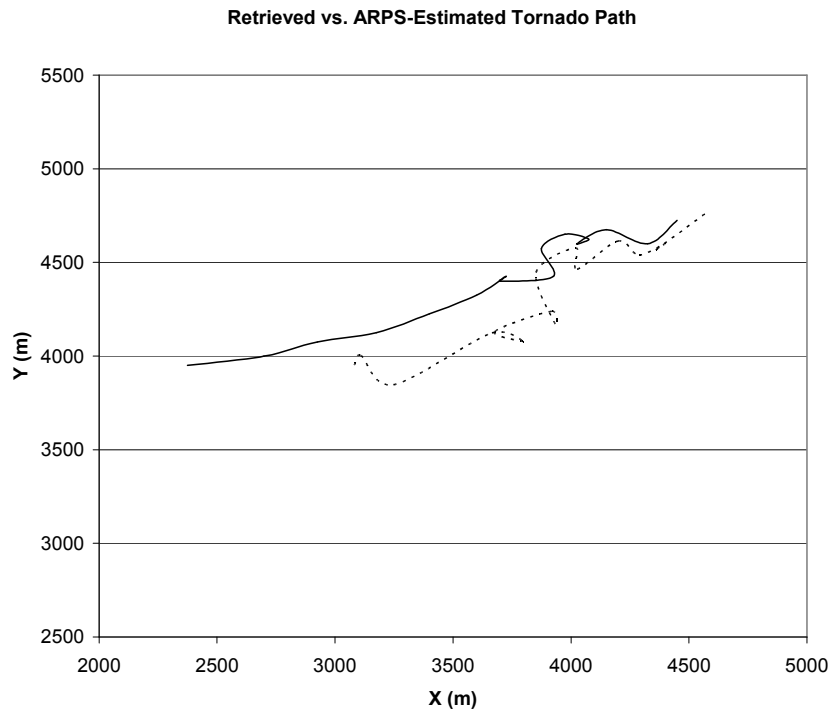


[Figure 10](#). ARPS-estimated tornado path (solid) and retrieved vortex path (dotted) over the sequence of 15 retrievals.

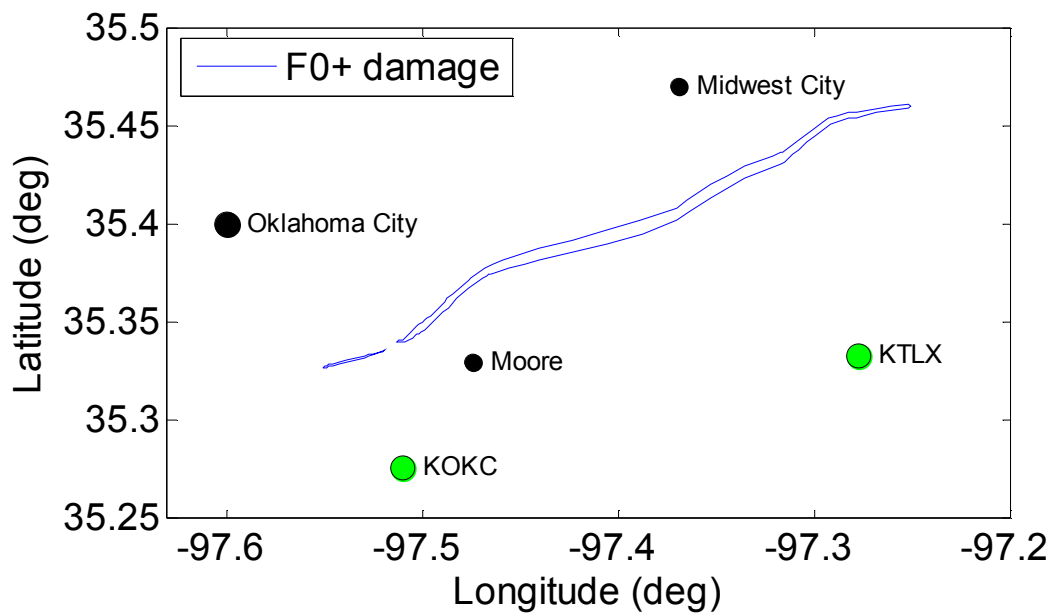
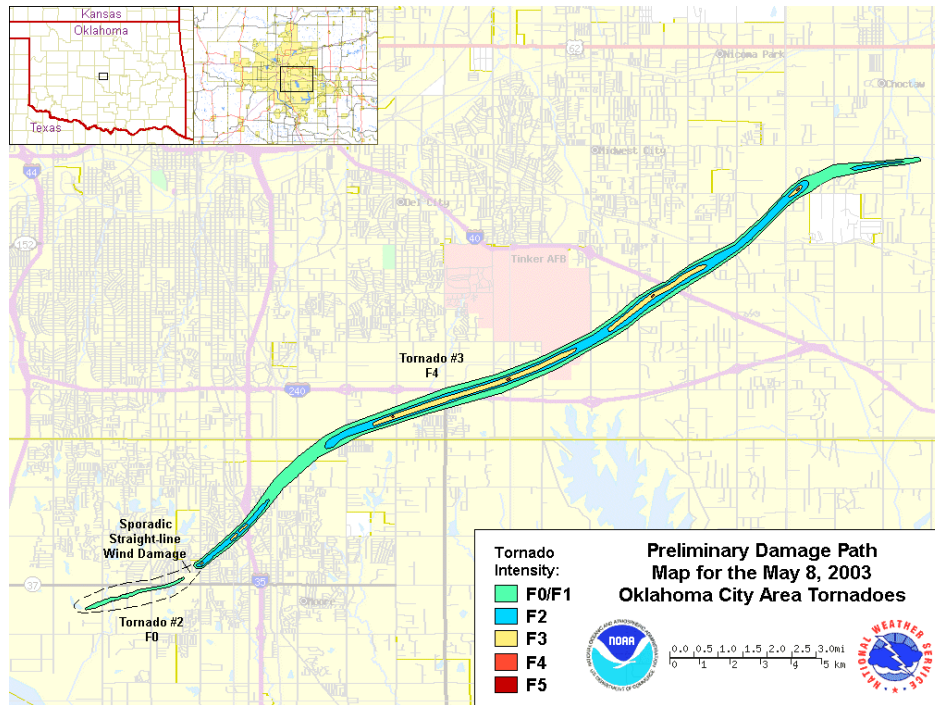
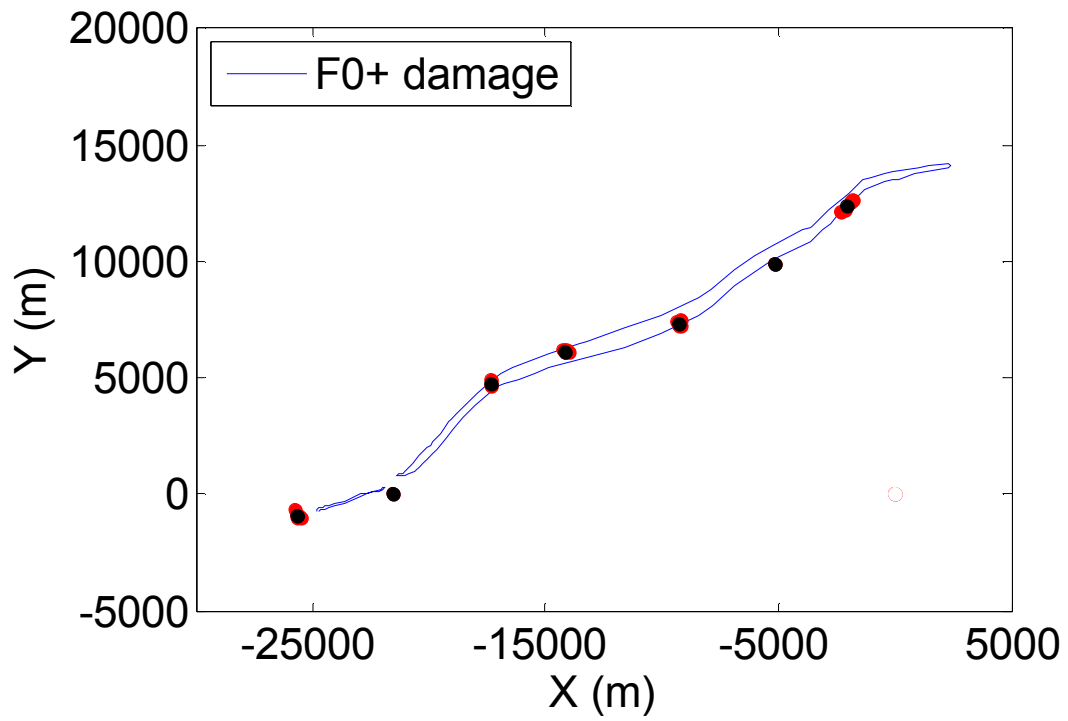


Figure 11. Damage path of 9 May 2003 Oklahoma City tornado (top; source: National Weather Service Warning and Forecast Office in Norman, OK) and relative locations of KOKC and KTLX (bottom).



[Figure 12](#). Retrieved individual (red dots) and ensemble mean (black dots) tornado locations overlaid with actual damage paths.

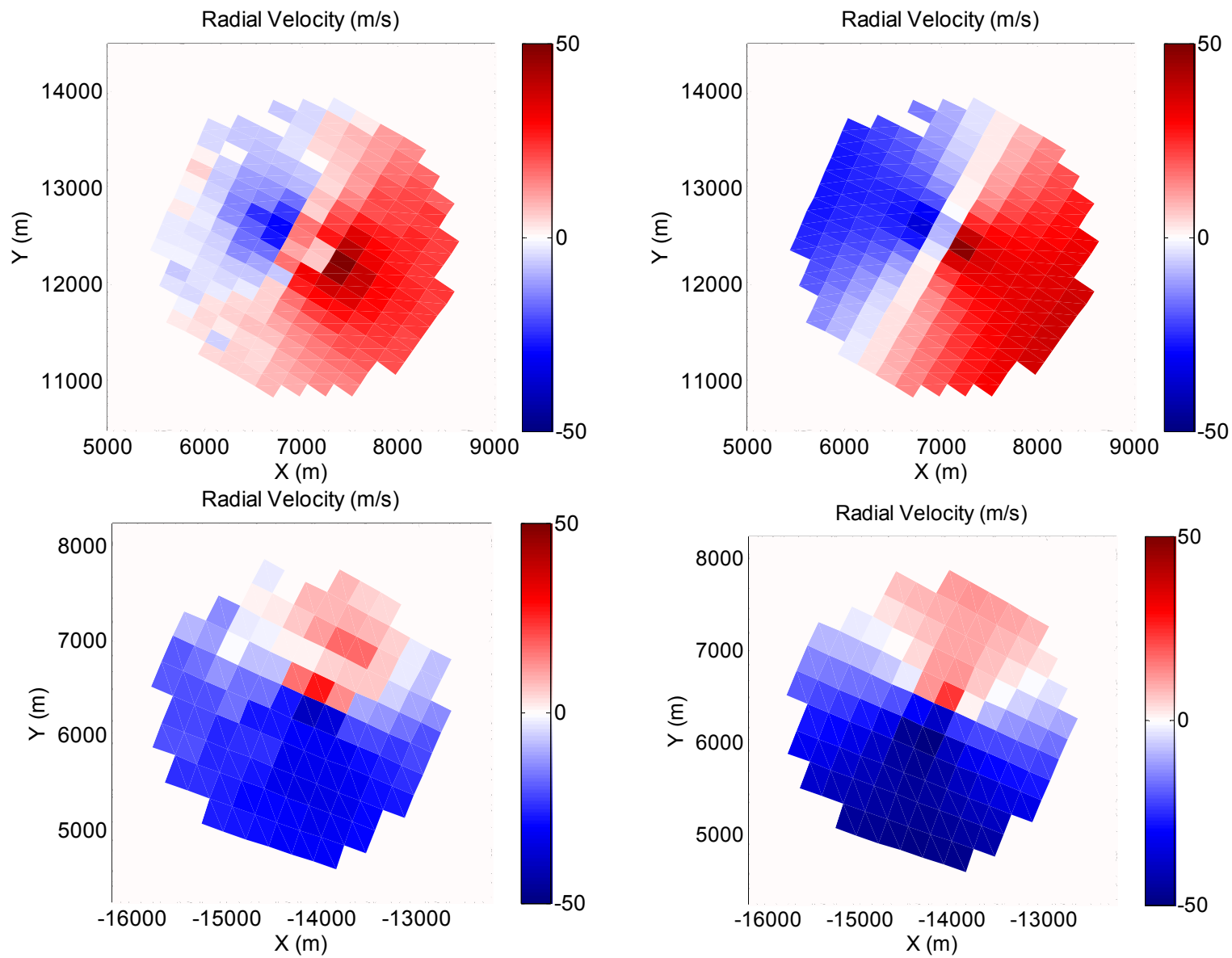
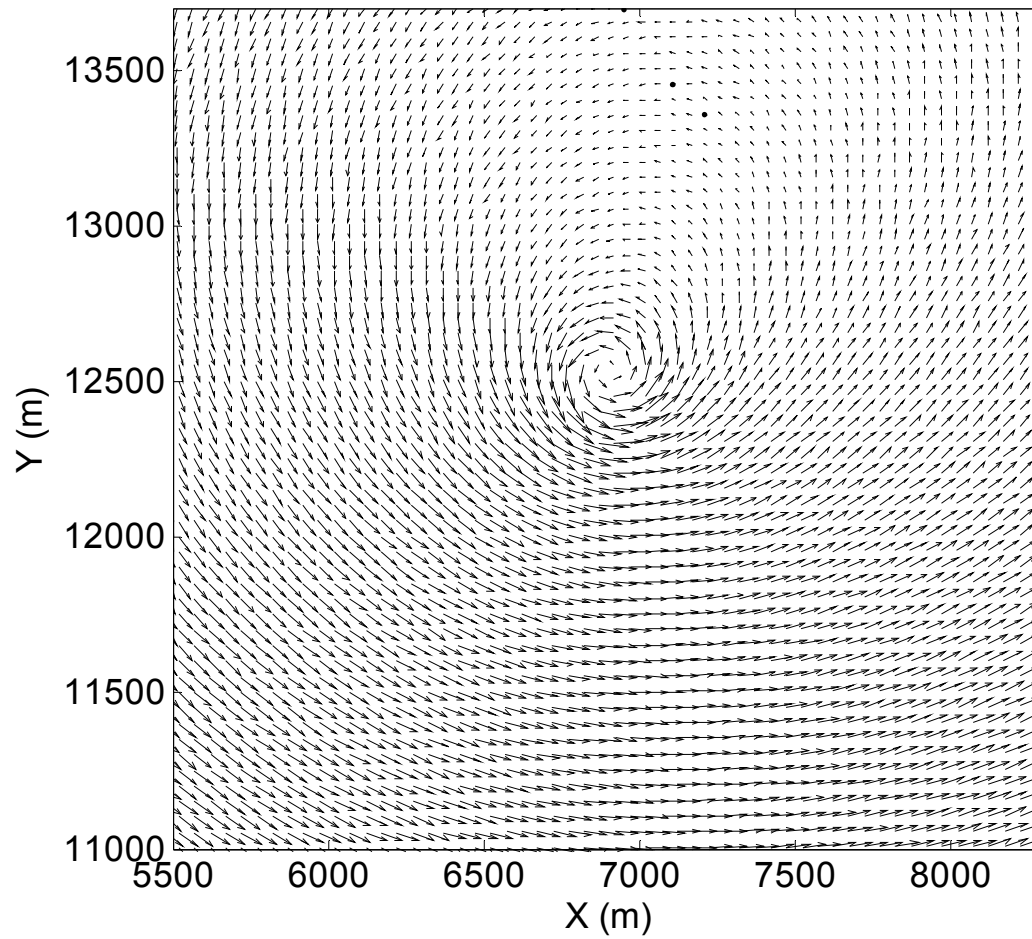


Figure 13. Observed (left) vs. retrieved (right) wind fields for KOKC (top) and KTLX (bottom) for a representative case.



[Figure 14](#). Representative example of a (total) wind field retrieved by the technique. Every other vector omitted for readability.